

X-RAY LUMINOSITY AND SIZE RELATIONSHIP OF SUPERNOVA REMNANTS IN THE LMC

PO-SHENG OU (歐柏昇),^{1,2} YOU-HUA CHU (朱有花),^{1,2,3} PIERRE MAGGI,⁴ CHUAN-JUI LI (李傳睿),^{1,2}
UN PANG CHANG (曾遠鵬),² AND ROBERT A. GRUENDL^{3,5}

¹*Institute of Astronomy and Astrophysics, Academia Sinica, P.O. Box 23-141, Taipei 10617, Taiwan, R.O.C.*
psou@asiaa.sinica.edu.tw

²*Department of Physics, National Taiwan University, Taipei 10617, Taiwan, R.O.C.*

³*Department of Astronomy, University of Illinois at Urbana-Champaign, 1002 West Green Street,
Urbana, IL 61801, U.S.A.*

⁴*Département d'Astrophysique, IRFU, CEA, Université Paris-Saclay, F-91191 Gif-sur-Yvette, France.*

⁵*National Center for Supercomputing Applications, 1205 West Clark St., Urbana, IL 61801, U.S.A.*

ABSTRACT

The Large Magellanic Cloud (LMC) has ~ 60 confirmed supernova remnants (SNRs). Because of the known distance, 50 kpc, the SNRs' angular sizes can be converted to linear sizes, and their X-ray observations can be used to assess X-ray luminosities (L_X). We have critically examined the LMC SNRs' sizes reported in the literature to determine the most plausible sizes. These sizes and the L_X determined from *XMM-Newton* observations are used to investigate their relationship in order to explore the environmental and evolutionary effects on the X-ray properties of SNRs. We find: (1) Small LMC SNRs, a few to 10 pc in size, are all of Type Ia with $L_X > 10^{36}$ ergs s⁻¹. The scarcity of small core-collapse (CC) SNRs is a result of CCSNe exploding in the low-density interiors of interstellar bubbles blown by their massive progenitors during their main sequence phase. (2) Medium-sized (10-30 pc) CC SNRs show bifurcation in L_X , with the X-ray-bright SNRs either in an environment associated with molecular clouds or containing pulsars and pulsar wind nebulae and the X-ray-faint SNRs being located in low-density interstellar environments. (3) Large (size > 30 pc) SNRs show a trend of L_X fading with size, although the scatter is large. The observed relationship between L_X and sizes can help constrain models of SNR evolution.

Keywords: ISM: supernova remnants — supernovae: general — X-rays: ISM — Magellanic Clouds

1. INTRODUCTION

Most supernova remnants (SNRs), regardless of progenitor types, exhibit some kind of X-ray emission. Thermal emission can arise from shocked interstellar medium (ISM) and/or SN ejecta, while relativistic electrons interacting with amplified magnetic field can produce non-thermal (synchrotron) emission. In the cases of core-collapse (CC) SNRs, there may exist additional X-ray emission from pulsars and pulsar wind nebulae (PWNe). See [Vink \(2012\)](#) for a comprehensive review of X-ray emission from SNRs.

To make a statistical study of X-ray emission of SNRs, we need a large sample of SNRs with known distances. The Galactic sample of SNRs is quite incomplete because of heavy absorption in the Galactic plane, and the distances to individual SNRs are often very uncertain. The Large Magellanic Cloud (LMC), on the other hand, has small internal and foreground absorption column densities ([Schlegel et al. 1998](#)), and hosts a large sample of SNRs all at essentially the same known distance 50 kpc¹ ([Pietrzyński et al. 2013](#)). At least 59 SNRs have been confirmed and a few additional SNR candidates have been suggested ([Maggi et al. 2016](#); [Bozzetto et al. 2017](#)). This large sample of LMC SNRs is ideal for systematic and statistical studies of X-ray emission from SNRs.

Recently, [Maggi et al. \(2016\)](#) analyzed *XMM-Newton* observations of the 59 confirmed SNRs in the LMC, deriving physical properties of the X-ray-emitting plasma from spectral fits. Because of the known distance, it is possible to determine the X-ray luminosity of each SNR. In the meantime, [Bozzetto et al. \(2017, hereafter Bo2017\)](#) measured the sizes of the 59 LMC SNRs using X-ray, radio and optical images. Intrigued by these results, we have examined the relationship between X-ray luminosity and size of LMC SNRs in order to explore evolutionary effects and environmental impacts on X-ray properties of SNRs.

This paper reports our investigation of the relationship between X-ray luminosity and size of SNRs in the LMC. In Section 2, we discuss the physical meaning of SNR sizes measured at optical or X-ray wavelengths, examine the SNR sizes reported in the literature, and assess the most reliable sizes that represent the SNRs' full extent. In Section 3, we plot X-ray luminosities against sizes for LMC SNRs and note intriguing fea-

tures in the distribution of SNRs in this plot. In Section 4, we discuss the physical reasons behind the distribution of SNRs in the plot of X-ray luminosity versus size. Finally, a summary is given in Section 5.

2. SIZES OF LMC SNRS

Both X-ray and optical images have been used to measure SNR sizes, but it should be noted that while X-ray and optical H α emission both originate from post-shock gas, they arise under different physical conditions. Generally speaking, X-ray emission comes from hot gas with temperatures $\gtrsim 10^6$ K, while H α emission originates from ionized gas at $\sim 10^4$ K; therefore, an SNR size measured in X-rays may differ from that measured in H α .

Measurements of X-ray and H α sizes of SNRs can also differ because of different instrumental sensitivities. For example, the *XMM-Newton* observations of the LMC SNRs detect volume emission measures ($EM_V \equiv \int n_e n_H dV$, where n_e is the electron density, n_H is the hydrogen density, and V is the emitting volume) of $10^{54} - 10^{60} \text{ cm}^{-3}$ ([Maggi et al. 2016](#)). For a spherical volume of highly ionized interstellar gas ($n_e/n_H \sim 1.2$ for a typical helium to hydrogen number ratio of 0.1), the rms density derived from the volume emission measure is

$$\langle n_H^2 \rangle^{1/2} = \left(\frac{5 EM_V}{\pi f D^3} \right)^{1/2}, \quad (1)$$

where D is the diameter of the X-ray emitting gas, and f is the volume filling factor. For SN ejecta dominated by heavy elements, n_e/n_H should be greater than 1.2, and hence the rms hydrogen density in equation (1) is the upper limit, which is about $(0.001-3) f^{-1/2} \text{ cm}^{-3}$ for the LMC SNRs as derived from the *XMM-Newton* measurements. Meanwhile, narrow-band H α CCD images can easily detect emission measures ($EM_\ell \equiv \int n_e n_H d\ell$, where ℓ is the emitting path length) down to $10-20 \text{ cm}^{-6}$ pc, and for an emitting path length of 5 pc the electron density needs to be at least $1.4-2 \text{ cm}^{-3}$. Thus, for SNRs running into a dense medium with densities $> 1 \text{ H-atom cm}^{-3}$, the shocked gas can be detected in both X-ray and optical wavelengths, while those running into a medium with densities $\ll 1 \text{ H-atom cm}^{-3}$ may be visible in X-rays but not in optical.

Another factor that can affect the measurements of SNR sizes is the wavelength-dependent confusion from the background. SNRs may be located adjacent to HII regions or superposed on a complex background, in which case the boundary of an SNR can be diagnosed by sharp filamentary morphology, enhanced [S II] line emission, high-velocity components in optical emission lines, nonthermal radio emission, and diffuse X-ray emission ([Chu 1997](#)). When more than one of the above diag-

¹ Note that due to the LMC's inclination of 18-23 degrees in the line of sight, the error in the distance and linear size can be uncertain by up to 10% ([Subramanian & Subramaniam 2010](#)), and the luminosity can be uncertain by 20%. These uncertainties, however, do not affect the general conclusions of these paper.

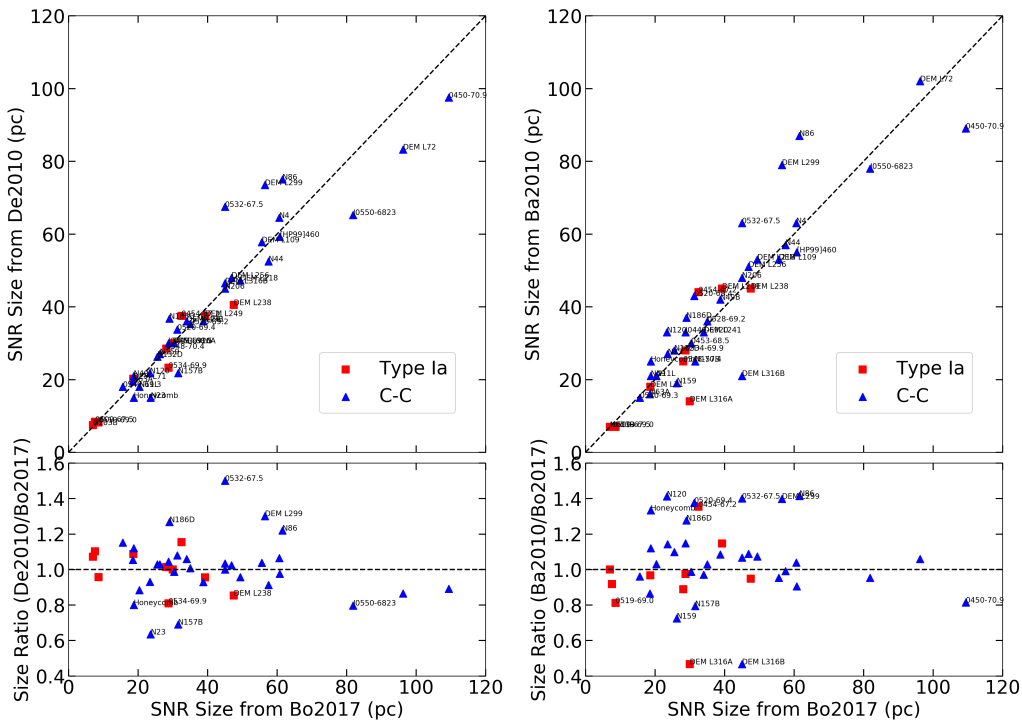


Figure 1. The left panels compare the SNR sizes reported by De2010 and Bo2017, with the upper panel plotting De2010 sizes versus Bo2017 sizes and the lower panel plotting the (De2010 size / Bo2017 size) ratios versus Bo2017 sizes. The right panels compare the SNR sizes reported by Ba2010 and Bo2017 in the same way as the left panels.

nostics are detected, the SNR boundary can be more reliably measured. However, if X-ray emission is the only diagnostic detected and the SNR emission is superposed on a large-scale diffuse X-ray emission, the background confusion can prevent accurate measurements of the SNR size.

Several publications have reported sizes of the LMC SNRs, but there are often discrepancies between their measurements. *Badenes et al. (2010, hereafter Ba2010)* used mainly X-ray images from *Chandra* or *XMM-Newton* to determine the SNR sizes, and adopted previous optical and radio measurements when high-resolution X-ray images were not available. *Desai et al. (2010, hereafter De2010)* considered optical and X-ray images, and measured SNR sizes based on the extent of diffuse X-ray emission or filamentary $H\alpha$ shell structure. Bo2017 considered optical, X-ray and radio images. *Maggi et al. (2016)* also listed SNR sizes, but they only gave the maximal diameters in X-ray; thus these sizes are often much larger than the ones reported by the above three references. Below we compare the SNR sizes reported by Ba2010, De2010, and Bo2017.

Bo2017 has the largest and most complete SNR sample, and is thus chosen to be the reference for comparisons. Figure 1 compares SNR sizes reported by De2010 and Bo2017 in the left panels, and Ba2010 and Bo2017 in the right panels. The upper panels plot SNR sizes

from one source versus another, while the lower panels plot the ratios of SNR sizes from two sources.

De2010 and Bo2017 both used primarily optical and X-ray images for the SNR size measurements, but there are still discrepancies greater than 16% and up to 50%. The discrepancies are caused by the following reasons: (1) The SNR sizes can be measured only in X-rays and the surface brightness varies significantly, such as N23, or the background is complex, such as the Honeycomb and 0532-67.5; in such cases the discrepancy in size measurements can be as high as 50%. (2) The SNR is superposed on an H II region or a superbubble, whose $H\alpha$ emission can confuse the size measurements, such as N157B and N186D. (3) The SNR size is measured without simultaneously considering optical, X-ray, and radio images that show wavelength-dependent distribution of emission, such as 0534-69.9, DEM L238, DEM L299, and J0550-6823. (4) The irregular shape of an SNR can cause subjective size measurements to differ by up to $\sim 20\%$, such as N86. For these discrepant objects, we examine their $H\alpha$, [S II], X-ray, and $24 \mu\text{m}$ images (in Appendix A), consider radio and kinematic properties available in the literature, and make new measurements (described in Appendix B).

The comparisons between Ba2010 and Bo2017 sizes, right panels of Figure 1, show numerous large discrepancies. These discrepancies are caused by the larger

uncertainties in Ba2010 sizes that were compiled from previous measurements based on mainly X-ray images and some optical images. As mentioned above and detailed in Appendices A–B, multi-wavelength examination of an SNR provides the most comprehensive picture of its physical structure and boundaries, and size measurements based on only one single wavelength may not reflect the SNR’s true extent.

3. RELATIONSHIP BETWEEN SIZES AND L_X

The LMC provides an ideal sample of SNRs for us to study the relationship between their X-ray luminosities (L_X) and sizes. The size of an SNR may be intuitively thought to reflect its evolutionary stage, because an SNR expands as the shock wave propagates outward and a large SNR would be older than a small SNR, if the ambient interstellar densities are similar. However, the ambient ISM does have a wide variety of physical properties and conditions, and the relationship between size and evolution can be quite complex. Through the relationship between L_X and size we hope to investigate effects of ambient environment and evolution on the SNRs’ X-ray luminosities.

SNRs rarely show round, symmetric shell structures with well-defined sizes. To assign a “size” to an irregular SNR, we adopt the average of its major and minor axes. Such SNR sizes determined from data of Ba2010, De2010, and Bo2017 are tabulated in Appendix C. As discussed at length in Section 2, De2010 and Bo2017 sizes were determined primarily with optical and X-ray images of SNRs and are in agreement for most cases. For 83% of the SNRs that have Bo2017 and De2010 sizes differ by less than 16%, we adopt their average sizes from Bo2017. For the SNRs with larger discrepancies between De2010 and Bo2017, we discuss individual objects and determine their average sizes in Appendix B, and list their adopted sizes in the table in Appendix C.

The LMC sample of SNRs have been studied in X-rays with *XMM-Newton* by Maggi et al. (2016). They fit the X-ray spectra with the package XSPEC (Arnaud 1996) using a combination of collisional ionization equilibrium (CIE) models and non-equilibrium ionization (NEI) models, derived their X-ray fluxes in the 0.3 to 8 keV band, and computed their L_X for an LMC distance of 50 kpc (Pietrzyński et al. 2013). These observed (absorbed) L_X are listed in the last column of the Table in Appendix C.

Using the L_X and average sizes in Appendix C, we plot the L_X versus size for the LMC SNRs in Figure 2. We have also made the same L_X –size plot with unabsorbed L_X and present it in Figure 3. (These unabsorbed L_X are from the same model fits that produced the absorbed

L_X published by Maggi et al. 2016). The distribution of the SNRs are qualitatively similar to that in Figure 2. Note that we did not include SN 1987A (size= 0.45 pc, $L_X = 2.7 \times 10^{36}$ ergs s⁻¹) because its inclusion will leave vast empty space on the left and compress all the data points on the right in Figure 2 and 3.

At first glance, the L_X – size plot for LMC SNRs shows a scattered diagram; however, if the sizes are divided into three ranges: <10 pc as “small”, 10–30 pc as “medium”, and >30 pc as “large”, it is possible to see interesting trends in each size range:

(1) For sizes a few to 10 pc, only a small group of SNRs exist with L_X of a few $\times 10^{36}$ ergs s⁻¹, and all of them are of Type Ia. For comparison, we add the Galactic SNRs with sizes a few to 10 pc in Figure 3; the data are taken from the Chandra Supernova Remnant Catalog². Interestingly, Tycho and Kepler SNRs, two small Type Ia SNRs in our Galaxy, are also located in the similar part of L_X –size plot as the small LMC Type Ia SNRs. In contrast, the Galactic CC SNR Cas A is an order of magnitude more luminous than these small Type Ia SNRs, and the ~ 100 -year old Galactic Type Ia SNR G1.9+0.3 is smaller and significantly fainter (Reynolds et al. 2008; Borkowski et al. 2010, 2013).

(2) For sizes 10–30 pc, there is a bifurcation in the distribution of SNRs. The X-ray-bright ones have $L_X > 10^{36}$ ergs s⁻¹ and the X-ray-faint ones have $L_X < 10^{35}$ ergs s⁻¹ for sizes below ~ 20 pc, and these two groups converge to a few $\times 10^{35}$ ergs s⁻¹ towards 30 pc size. It is worth noting that the X-ray-faint medium-sized SNRs are mostly CC SNRs.

(3) For sizes >30 pc, while L_X exhibits a wide range, the majority of the SNRs appear to show a general trend of L_X decreasing with size.

It also appears that the Type Ia SNRs show smaller scatter in L_X for any given size than the CC SNRs, especially in the medium size range (Figures 2 and 3). The scatter in L_X reflects the ambient interstellar density: Type Ia SNe occur in diffuse medium with moderate densities, while CC SNe can take place near dense molecular clouds or in a very low-density environment produced by energy feedback from massive stars. Because of the smaller scatter in L_X , the smooth variations of Type Ia SNRs’ L_X versus size may demonstrate the SNR evolution.

The dashed line in the lower right corner of Figure 2 corresponds to a constant surface brightness of 10^{29} ergs s⁻¹ arcsec⁻², which represents the typical detection limit of the *XMM-Newton* observations used by Maggi et

² See <http://hea-www.cfa.harvard.edu/ChandraSNR/>.

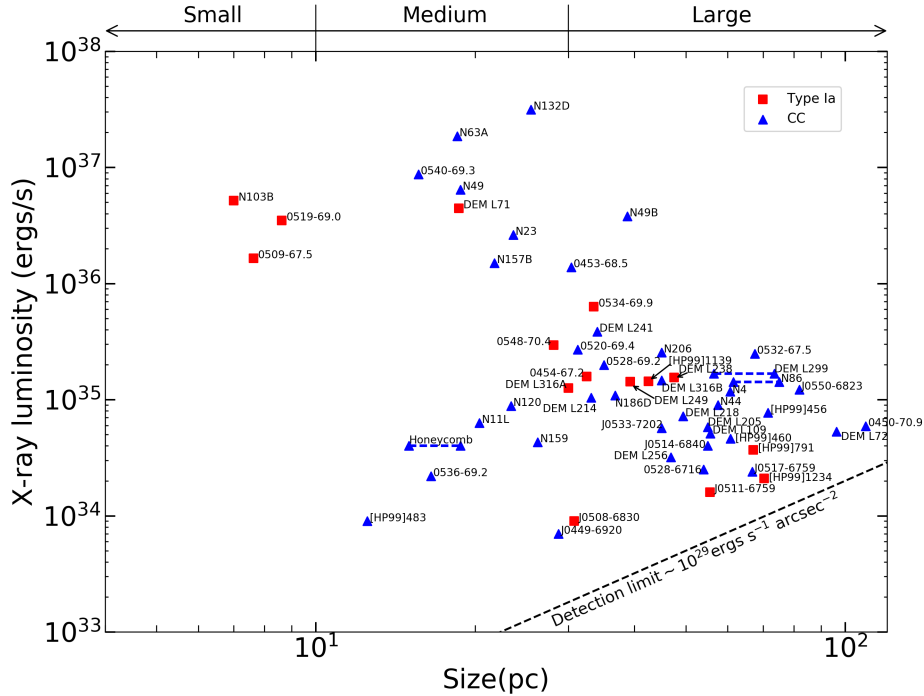


Figure 2. Observed L_X versus size plot for SNRs in the LMC. The size and L_X are listed in Appendix C. For the Honeycomb SNR and N86, we have used two extreme size measurements to illustrate the largest uncertainties in the size measurements. Note that some of the large CC SNRs may in fact be Type Ia SNRs whose SN ejecta have cooled and no longer emit detectable X-rays for them to be identified as such.

al. (2016). Consequently, no SNRs are located beneath this dashed line.

4. DISCUSSION

We have examined the physical structures and environments of SNRs in the three size ranges in order to understand the physical significance of their distributions in the L_X -size plot. The discussion in this section is ordered according to the SNR sizes.

4.1. Small Known LMC SNRs Are Dominated by Type Ia

It is striking that the small LMC SNRs, with sizes a few to 10 pc, are all Type Ia SNRs with L_X of a few $\times 10^{36}$ ergs s^{-1} . (Note that SN 1987A is outside the size range under discussion.) For comparison, we show that the Galactic Type Ia SNRs Kepler and Tycho are both located in a similar region as the young LMC Type Ia SNRs. The small range of L_X for small Type Ia SNRs and the scarcity of small CC SNRs can be explained as follows.

Type Ia SNe are usually considered to explode in a tenuous and uniform ISM (e.g., Badenes et al. 2005). On the other hand, CC SNe usually explode inside interstellar bubbles blown by the fast stellar winds of their mas-

sive progenitors during the main sequence phase (Castor et al. 1975; Weaver et al. 1977). Interstellar bubble interiors have very low densities, and hence CC SNe inside bubbles are called “cavity explosions”. It is conceivable that the interstellar environments of Type Ia and CC SNe have very different density profiles.

Density profiles of ambient medium strongly affect the evolution of an SNR’s L_X . In a classical model of a SN explosion in a uniform ISM, the resulting SNR goes through free expansion phase, Sedov phase (i.e., adiabatic phase), and radiative phase (Woltjer 1972). The Sedov phase starts when the swept-up ISM mass is several times the SN ejecta mass (e.g., Dwarkadas & Chevalier 1998). The L_X of an SNR during the Sedov phase can be calculated (e.g., Hamilton et al. 1983). To illustrate the evolution of L_X for different ambient densities, we plot L_X against age and size in Figure 4.

For a Type Ia SNR in a partially neutral ISM, only the ionized interstellar gas can be swept up by the shock. Thus, for a uniform density of ~ 1 H-atom cm^{-3} and a neutral fraction of η , the Sedov phase will start when the swept-up ionized gas reaches $1.4 M_\odot$ in mass, corresponding to a radius of $2.4(1-\eta)^{-1/3}$ pc. This radius is 5.2 pc if $\eta = 0.9$, and 3 pc if $\eta = 0.5$. These sizes are comparable to the young Balmer-dominated Type

the forward shock in an interstellar shell well resolved from the reverse shock in the SN ejecta (Hughes et al. 2003; Hendrick et al. 2003).

X-ray emission from reverse shocks is the cause of the high L_X of small Type Ia SNRs. The small scatter of these young bright Type Ia SNRs in the L_X vs size plot reflects their similar ages, the relative uniformity of SNe Ia (in term of nucleosynthesis and explosion energy), and the modest effect the progenitors have on changing their immediate surrounding. The smallest Galactic Type Ia SNR G1.9+0.3 has a low L_X because it is so young (<200 yr) that the reverse shock has only gone through very little of the SN ejecta (Reynolds et al. 2008; Borkowski et al. 2014).

For CC SNRs whose SNe exploded in cavities of wind-blown bubbles, due to the extremely low density within the bubbles ($\sim 10^{-4} - 10^{-2}$ H-atom cm^{-3}), the X-ray emission from shocked gas would be too faint to be detected at a young age; only when the SNR’s forward shock hits the dense shell/wall of a bubble will the X-ray luminosity jump up several orders of magnitude (Dwarkadas 2005). As shown by Nazé et al. (2001), main sequence O stars have interstellar bubbles of sizes 15–20 pc. By the time a massive star explodes as a CC SN, its main-sequence bubble has grown larger, and hence the SNR shock goes through the low-density bubble interior without producing detectable X-ray emission until it hits the bubble shell wall at radius of 10 pc or larger.

For illustration, considering a spherical interstellar bubble with a radius of 10 pc and assuming a simplistic extreme case (upper limit) of average density of 0.01 H-atom cm^{-3} in the bubble interior, we can calculate the total mass in the bubble interior to be $\lesssim 1 M_\odot$; thus, when the SNR shock reaches the bubble wall, it has swept up only $\sim 1 M_\odot$, much lower than the CCSN ejecta mass, a few to a few tens M_\odot ; thus, the Sedov phase has not been reached. The bubble shell consists of swept-up ISM that was originally distributed in the bubble cavity. Assuming the bubble was blown in a diffuse ISM with density of 1 H-atom cm^{-3} , the total mass in the bubble shell would be 100 M_\odot ; therefore, the SNR reaches the Sedov phase when the forward SNR shock traverses the bubble shell.

During the free-expansion phase, the SNR shock is not significantly decelerated and it remains fast until it hits the bubble wall. Assuming a constant shock velocity of 10,000 km s^{-1} , it only takes 1000 years for the SNR to grow to a radius of 10 pc. Consequently, SNRs inside interstellar bubbles not only emit very faintly in X-rays, but also expand very rapidly to reach the dense shell wall. Such “cavity explosions” explain the absence of small CC SNRs in the L_X -size plot. Cavity explosions

are also responsible for the discrepancies between ionization ages and dynamical ages of LMC SNRs, such as N132D, N63A, and N49B (Hughes et al. 1998).

We have plotted the young CC SNR Cas A in Figure 3 for comparison. Cas A is small in size and luminous in X-rays. These properties are caused by its interaction with a dense circumstellar medium, i.e., material ejected by the SN progenitor (Fesen 2001). Circumstellar bubbles are often observed around Wolf-Rayet stars and luminous blue variables (LBVs), and circumstellar bubbles are smaller than interstellar bubbles (Chu 2003). Cas A SN must have exploded in a circumstellar bubble.

4.2. X-ray-Bright and X-ray-Faint Medium-Sized SNRs

The medium-sized LMC SNRs show clear bifurcation in their L_X . In the X-ray-bright group with $L_X \geq 10^{36}$ ergs s^{-1} , only one is of Type Ia, and the other seven are CC SNRs. Among these X-ray-bright CC SNRs, four are interacting with molecular clouds, as CO emission was detected near the SNRs N23, N49, and N132D (Banas et al. 1997; Park et al. 2003) and H_2 absorption is detected in *Spitzer* IRS observations towards N63A (Segura-Cox et al. 2018, in preparation). None of these four X-ray-bright CC SNRs show sharp $\text{H}\alpha$ shell structure enclosing the diffuse X-ray emission, indicating that the forward SNR shocks are still in the low-density interiors of bubbles. In the cases of N23 and N132D, where no prominent shocked cloudlets are seen, the X-ray emission does show limb-brightening, indicating that the ambient medium is dense enough to produce detectable X-ray emission but not optical $\text{H}\alpha$ emission, and this ambient medium may correspond to the conduction layer in a bubble interior (Weaver et al. 1977). As N23 and N132D are both associated with molecular clouds, their bubble shells and conduction layers must have higher densities, which contribute to the bright X-ray emission. In the cases of N49 (Bilikova et al. 2007; Park et al. 2012) and N63A (Warren et al. 2003), it is clear that dense cloudlets, possibly associated with the molecular clouds, have been shocked and contribute to the X-ray emission. The other three X-ray-bright CC SNRs possess bright PWNe: 0540–69.3 (Gotthelf & Wang 2000), N157B (Wang & Gotthelf 1998), and 0453–68.5 (Gaensler et al. 2003). Pulsars and PWN are powerful sources of nonthermal X-ray emission and provide additional X-ray emission to boost their SNRs’ total L_X . Note that the PWN of 0453–68.5 is not particularly dominating, but its X-ray image show a limb-brightened sharp shell that indicates that the shock has already reached the bubble shell. While 0453–68.5 has

a PWN, it is the SNR shock impact on the dense bubble shell giving rise to L_X .

The X-ray-faint medium-sized SNRs are mostly associated with CC SNe. Among the three X-ray-faint CC SNRs smaller than 20 pc, 0536–69.2 and [HP99]483 are not detected in optical, and the Honeycomb SNR shows only a small patch of honeycomb-like nebulosity resulting from SNR shocking a piece of shell wall (Chu et al. 1995; Meaburn et al. 2010). The absence of sharp optical shells enclosing the diffuse X-ray emission indicates a low-density ISM around these SNRs. The Honeycomb SNR has hit a small piece of dense gas and hence it has the highest L_X among these three, but still a couple orders of magnitude fainter than the SNRs interacting with molecular clouds. The X-ray-faint SNRs with sizes 20–30 pc all show optical shell structure enclosing their diffuse X-ray emission, and they have higher L_X than the smaller ones, except J0449–6920, whose *XMM-Newton* observation was too shallow to make accurate measurements. These CC SNRs may represent cavity explosions whose SNR shocks have just reached the bubble shell walls. The SNRs N11L and N120 have just reached the bubble shell, but the bubble shell densities are not as high as those of N23 and N132D.

4.3. Fading of X-rays in Large SNRs

Among the large (size >30 pc) LMC SNRs, a general trend of decreasing L_X for larger SNRs can be seen, but for any given size, the differences in L_X can be up to one order of magnitude.

As an SNR sweeps up more interstellar gas, the shock velocity decreases and when it goes much below ~ 300 km s⁻¹, the post-shock temperature will be below 10^6 K, too low to generate X-ray-emitting gas. The hot gas in SNR interior cools, and the X-ray emission diminishes.

The scatter in L_X may be caused by the differences in ambient gas densities (n_0) and the SN explosion energies (E). To evaluate the effects of these two factors, we consider a spherical SNR of radius R , whose X-ray emission originates from shocked ISM in a shell. Its L_X is \propto (emitting volume) \times (density)² \times (emissivity). As (emitting volume) \times (density) is proportional to the total interstellar mass within radius R , it is $\propto R^3 n_0^2$. The emissivity is a slow function of temperature for photon energies below 2 keV (Hamilton et al. 1983). Since the large old SNRs are likely at low X-ray emitting temperatures, a few $\times 10^6$ K at most, we will treat the emissivity as a constant, and $L_X \propto R^3 n_0^2$.

The total kinetic energy in the SNR shell scales with the explosion energy, so $E \propto R^3 n_0 v^2$. The large old SNRs have low expansion velocities of a few $\times 10^2$ km s⁻¹, so we will also approximate the expansion velocity

as a constant. Thus, $L_X \propto E n_0^3$. The effects of the ambient density and the SN explosion energy are about equally important. However, the ranges of the ambient gas densities and the SN explosion energies are quite different. The ambient interstellar density can range from 0.01 to a few hundred H-atom cm⁻³, about 4 orders of magnitude, while the SN explosion energies are mostly clustered around 10^{51} ergs with extreme values differing by no more than 3 orders of magnitude (e.g., Woosley & Weaver 1986).

Hence, the large scatter in L_X for SNRs with the same size is more likely caused by the detailed differences in the ambient gas densities, and the SN explosion energy plays a lesser role in raising the scatter in L_X .

5. SUMMARY

The LMC is at a known distance of 50 kpc, and thus the linear sizes of SNRs in the LMC can be determined from their angular size measurements (Desai et al. 2010; Bozzetto et al. 2017), and their X-ray luminosities can be determined from *XMM-Newton* X-ray observations (Maggi et al. 2016), allowing a unique opportunity to examine the relationship between L_X and size of SNRs. We have critically compared LMC SNR sizes reported by different authors in the literature and adopted the most reasonable sizes to investigate how L_X vary with sizes among the LMC sample of SNRs.

We find that the L_X – size relationship for LMC SNRs can be divided into small, medium, and large size ranges: (1) The small LMC SNRs with sizes a few to 10 pc are all young Type Ia SNRs with L_X a few times 10^{36} ergs s⁻¹. The apparent scarcity of small CC SNRs may be caused by their “cavity explosions”, as massive progenitors of CCSNe have blown interstellar bubbles and the SN explosions take place in the very low-density interiors of the bubbles.

(2) The medium-sized SNRs, with sizes 10–30 pc, show bifurcation in their L_X with an order of magnitude difference in L_X . The X-ray-bright CC SNRs either are in an environment associated with molecular clouds or have pulsars and pulsar-wind nebulae emitting nonthermal X-ray emission.

(3) The large SNRs, with sizes greater than ~ 30 pc, show a general trend of fading L_X at large sizes. As these sizes are larger than the normal interstellar bubbles blown by massive stars, the large SNRs have swept up the bubble material and extended into the diffuse

³ Note that this is in interesting contrast with the radio luminosity, which scales as $L_{radio} \propto E^{1.3} n_0^{0.45}$ or $L_{radio} \propto E^{1.45} n_0^{0.3}$ depending on the magnetic field amplification mechanism by the shock (Chomiuk & Wilcots 2009).

ISM. As the SNR shocks sweep up more ISM, the shock velocity slows down. When the post-shock velocities are too low to produce X-ray-emitting material, the hot plasma in SNR interiors cool and reduce the X-ray emission.

This project is supported by Taiwanese Ministry of Science and Technology grant MOST 104-2112-M-001-044-MY3.

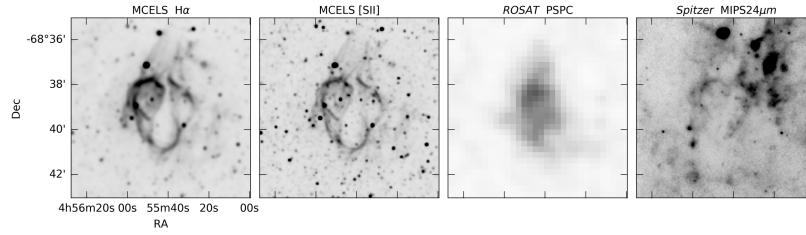
REFERENCES

- Arnaud, K. A. 1996, *Astronomical Data Analysis Software and Systems V*, 101, 17
- Badenes, C., Maoz, D., & Draine, B. T. 2010, *MNRAS*, 407, 1301
- Badenes, C., Borkowski, K. J., & Bravo, E. 2005, *ApJ*, 624, 198
- Banas, K. R., Hughes, J. P., Bronfman, L., & Nyman, L.-Å. 1997, *ApJ*, 480, 607
- Bilikova, J., Williams, R. N. M., Chu, Y.-H., Gruendl, R. A., & Lundgren, B. F. 2007, *AJ*, 134, 2308
- Borkowski, K. J., Reynolds, S. P., Green, D. A., et al. 2014, *ApJL*, 790, L18
- Borkowski, K. J., Reynolds, S. P., Hwang, U., et al. 2013, *ApJL*, 771, L9
- Borkowski, K. J., Reynolds, S. P., Green, D. A., et al. 2010, *ApJL*, 724, L161
- Bozzetto, L. M., Filipović, M. D., Vukotić, B., et al. 2017, *ApJS*, 230, 2
- Bozzetto, L. M., Filipovic, M. D., Crawford, E. J., et al. 2012, *RMxAA*, 48, 41
- Castor, J., McCray, R., & Weaver, R. 1975, *ApJL*, 200, L107
- Chomiuk, L., & Wilcots, E. M. 2009, *ApJ*, 703, 370
- Chu, Y.-H. 2003, *A Massive Star Odyssey: From Main Sequence to Supernova*, 212, 585
- Chu, Y.-H. 1997, *AJ*, 113, 1815
- Chu, Y.-H., Dickel, J. R., Staveley-Smith, L., Osterberg, J., & Smith, R. C. 1995, *AJ*, 109, 1729
- Chu, Y.-H., Kennicutt, R. C., Jr., Schommer, R. A., & Laff, J. 1992, *AJ*, 103, 1545
- Desai, K. M., Chu, Y.-H., Gruendl, R. A., et al. 2010, *AJ*, 140, 584
- Dwarkadas, V. V. 2005, *ApJ*, 630, 892
- Dwarkadas, V. V., & Chevalier, R. A. 1998, *ApJ*, 497, 807
- Fesen, R. A. 2001, *ApJS*, 133, 161
- Gaensler, B. M., Hendrick, S. P., Reynolds, S. P., & Borkowski, K. J. 2003, *ApJL*, 594, L111
- Gotthelf, E. V., & Wang, Q. D. 2000, *ApJL*, 532, L117
- Hamilton, A. J. S., Sarazin, C. L., & Chevalier, R. A. 1983, *ApJS*, 51, 115
- Hendrick, S. P., Borkowski, K. J., & Reynolds, S. P. 2003, *ApJ*, 593, 370
- Hughes, J. P., Ghavamian, P., Rakowski, C. E., & Slane, P. O. 2003, *ApJL*, 582, L95
- Hughes, J. P., Hayashi, I., & Koyama, K. 1998, *ApJ*, 505, 732
- Kosenko, D., Helder, E. A., & Vink, J. 2010, *A&A*, 519, A11
- Laval, A., Rosado, M., Boulesteix, J., et al. 1989, *A&A*, 208, 230
- Maggi, P., Haberl, F., Kavanagh, P. J., et al. 2016, *A&A*, 585, A162
- Meaburn, J., Redman, M. P., Boumis, P., & Harvey, E. 2010, *MNRAS*, 408, 1249
- Nazé, Y., Chu, Y.-H., Points, S. D., et al. 2001, *AJ*, 122, 921
- Park, S., Hughes, J. P., Slane, P. O., et al. 2012, *ApJ*, 748, 117
- Park, S., Burrows, D. N., Garmire, G. P., et al. 2003, *ApJ*, 586, 210
- Pietrzyński, G., Graczyk, D., Gieren, W., et al. 2013, *Nature*, 495, 76
- Reynolds, S. P., Borkowski, K. J., Green, D. A., et al. 2008, *ApJL*, 680, L41
- Schlegel, D. J., Finkbeiner, D. P., & Davis, M. 1998, *ApJ*, 500, 525
- Sedov, L. I. 1959, *Similarity and Dimensional Methods in Mechanics*, New York: Academic Press, 1959,
- Subramanian, S., & Subramaniam, A. 2010, *A&A*, 520, A24
- Taylor, G. 1950, *Proceedings of the Royal Society of London Series A*, 201, 159
- Vink, J. 2012, *A&A Rv*, 20, 49
- Wang, Q. D., & Gotthelf, E. V. 1998, *ApJ*, 494, 623
- Warren, J. S., & Hughes, J. P. 2004, *ApJ*, 608, 261
- Warren, J. S., Hughes, J. P., & Slane, P. O. 2003, *ApJ*, 583, 260
- Warth, G., Sasaki, M., Kavanagh, P. J., et al. 2014, *A&A*, 567, A136
- Weaver, R., McCray, R., Castor, J., Shapiro, P., & Moore, R. 1977, *ApJ*, 218, 377
- Williams, R. M., Chu, Y.-H., Dickel, J. R., et al. 1999, *ApJS*, 123, 467
- Woltjer, L. 1972, *ARA&A*, 10, 129
- Woosley, S. E., & Weaver, T. A. 1986, *ARA&A*, 24, 205

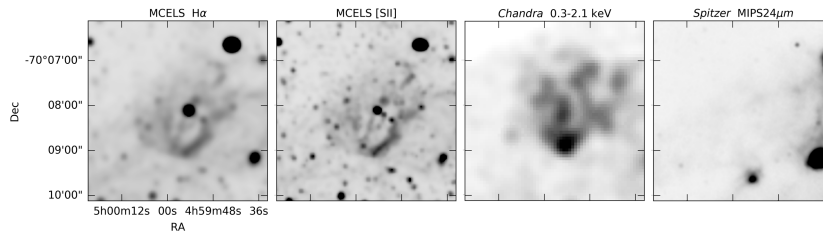
APPENDIX

A. IMAGES OF THE SNRS WITH LARGE DISCREPANCIES BETWEEN DIFFERENT SIZE MEASUREMENTS

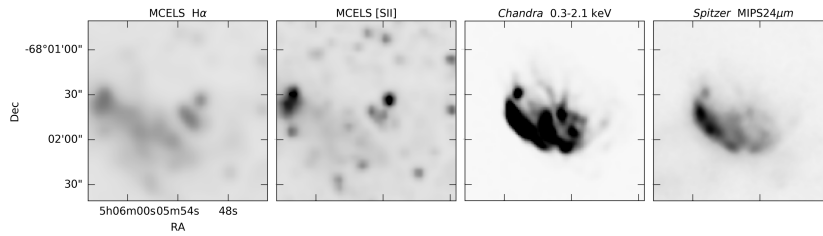
N86



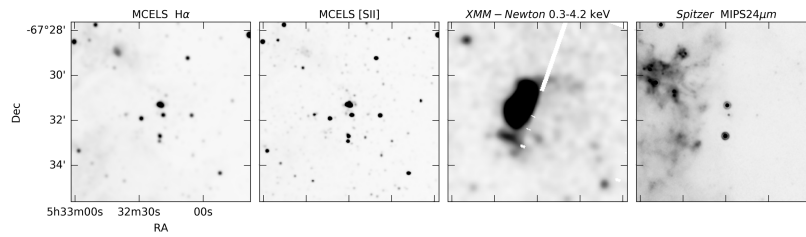
N186D



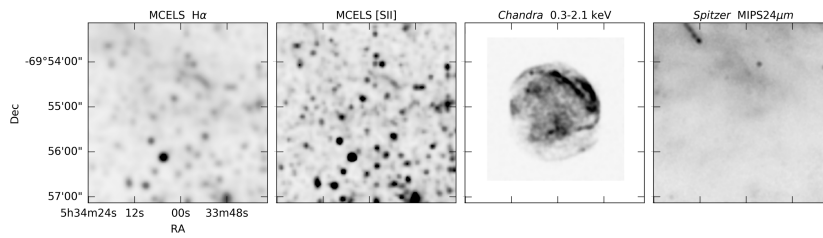
N23



SNR 0532-67.5



SNR 0534-69.9



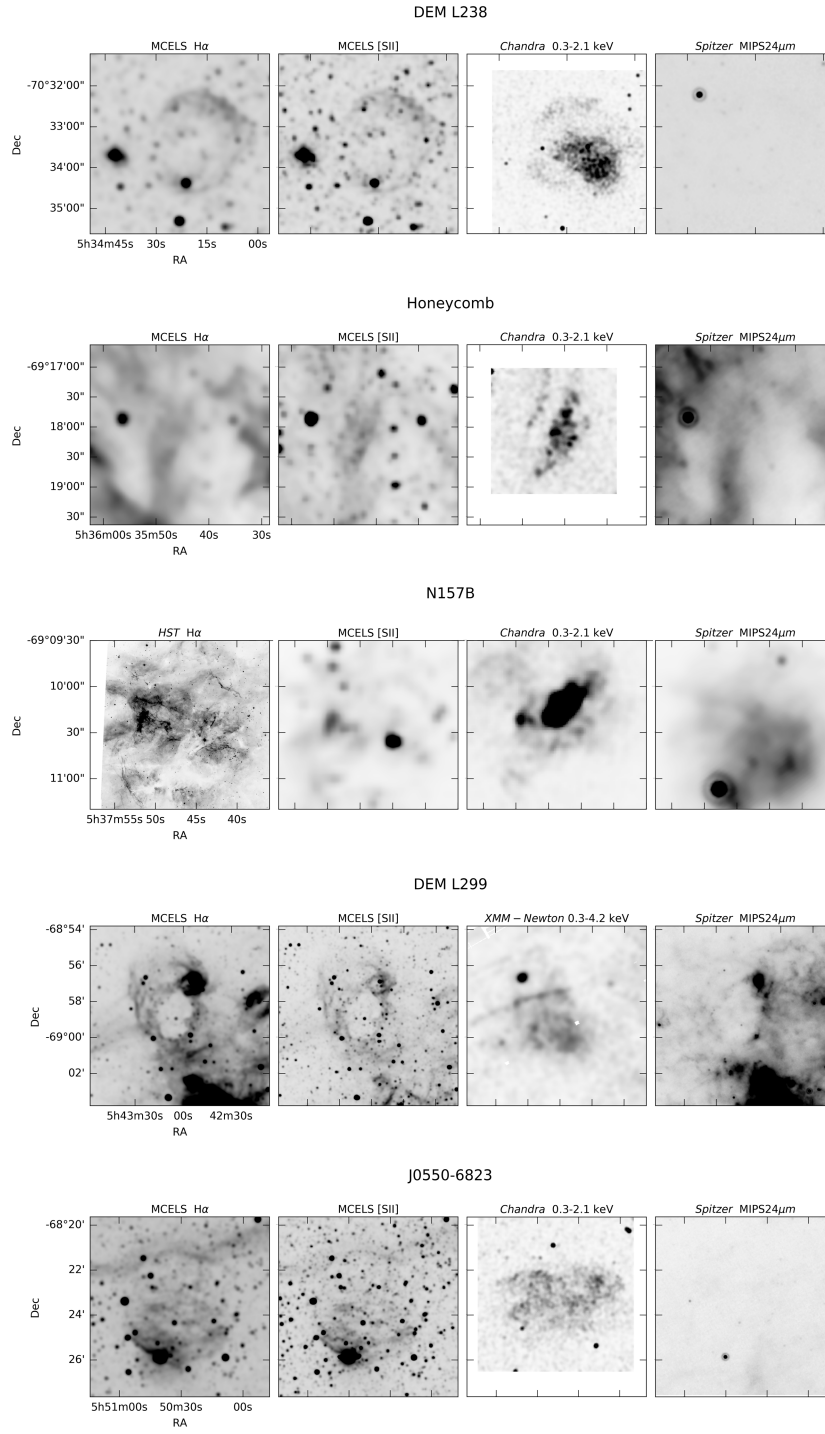


Figure 5. Images of the SNRs with large discrepancies between the size measurements of Bo2017 and De2010.

B. DESCRIPTIONS OF SIZE DETERMINATIONS FOR INDIVIDUAL SNRS

N86.– The shape of the SNR is irregular because of the breakout structure in the north, through which the hot gas flows out from the SNR shell (Williams et al. 1999). For N86 in Figure 2, we have used both sizes of De2010 (75.0 pc, including the breakout) and Bo2017 (61.5 pc, not including the breakout) in the L_X – size plot to illustrate the uncertainty in the size. Only low-resolution *ROSAT* X-ray images are available for N86; high-resolution *Chandra* and *XMM-Newton* observations will help refine the size determination.

N186D.– The size of SNR N186D in $H\alpha$ cannot be unambiguously measured, because N186D is projected on the rim of the superbubble N186E. Through the analysis of velocity fields in N186D, Laval et al. (1989) determined the SNR size to be ~ 40 pc, which is consistent with the size of the [S II]-enhanced shell (see Figure 5 in Appendix A). Based on these considerations, we adopt the size 36.8 pc given by De2010.

N23.– X-ray emission of N23 is enhanced in the southeast side, likely due to a denser ambient medium (Williams et al. 1999). The size reported by De2010, 18×12 pc, corresponds to only the X-ray-brightest region. Maggi et al. (2016) and Bo2017 included the fainter X-ray emission from the northwest side and reported a larger SNR size, 23.6 pc, which is more accurate and hence adopted in the L_X –size plot in Figure 2.

SNR 0532-67.5.– This SNR may be associated with the OB association LH75 (Chu 1997). This SNR has no optical counterpart, indicating that it is in a low-density medium, possibly caused by the fast stellar winds and SN explosions from LH75. The size of this SNR can be measured only in X-rays. There is bright X-ray emission in a $\sim 40 \times 20$ pc region, and a fainter and larger X-ray arc connected with the bright region. As in the case of the SNR N23, we include both the bright and faint X-ray emission regions in the size estimate, and adopt a size of 67.5 pc as the size of SNR 0532-67.5.

SNR 0534-69.9.– The optical images of this SNR show only a faint filament associated with the brightest X-ray emission region. *Chandra* observations show the SNR clearly in X-rays, although the southern rim is much fainter than the rest of the SNR. We have measured and adopted the full extent of the SNR shown in X-rays, about 33.5 pc, similar as the size measured by Maggi et al. (2016), which is larger than those reported by De2010 and Bo2017.

DEM L238.– Comparing $H\alpha$ and *Chandra* images, the X-ray emitting region is larger than the optical shell. We adopt the full extent of the SNR, 47.5 pc.

Honeycomb.– The Honeycomb SNR is near the 30 Doradus complex, and to the south of the superbubble 30 Dor C. This region has a very complex star formation history and chaotic nebular morphology. The lack of bright ionized gas region suggests an evolved environment with low ISM densities. The optical morphology of the SNR is very irregular, consisting of many cells instead of a simple shell (Chu et al. 1995; Meaburn et al. 2010), leading to large uncertainty in the determination of SNR size. For the Honeycomb SNR, we have used both sizes of De2010 (15 pc) and Ba2010 (25.5 pc) in the L_X – size plot to illustrate the uncertainty in the size.

N157B.– The environment of N157B in $H\alpha$ is very complex because this SNR is superposed on the HII region of the OB association LH99 (Chu 1997), and dissected by a foreground dark cloud. The most reliable measurement of the SNR size is through the analysis of gas kinematics using long-slit high-dispersion spectroscopic observations, 25×18 pc (Chu et al. 1992). This SNR boundary has been confirmed by sharp filaments revealed by *HST* images as shown in Figure 5. The size 21.8 pc given by De2010 is taken from Chu et al. (1992).

DEML299.– This SNR is inside a large optical shell. The size reported by De2010 corresponds to the large optical shell. The X-ray emission actually extends from the shell cavity to the southwest, indicating an outflow. The [S II]/ $H\alpha$ ratio is enhanced in the shell structure and in the superposed filaments of supergiant shell LMC-2. The SNR is clearly in a very complex environment. We include all the diffuse X-ray emission region and [S II] enhanced filaments, and measure a size of 100×50 pc. A smaller SNR size, ~ 55 pc, has been reported by Warth et al. (2014) and Maggi et al. (2016) based on the diffuse X-ray emission and a surrounding [S II]-enhanced filament. The large discrepancy between these two size measurements illustrate the difficulty in determining SNR sizes in a complex environment confused by other energetic feedback processes from massive stars. We adopt both 73.5 and 56.5 pc in Table 1 (Appendix C) and Figure 2.

J0550-6823.– While the diameter of the optical shell is only ~ 68 pc, there is X-ray and radio emission extending over 90 pc in the east-west direction; therefore, we adopt the size of 90×68 pc by Bozzetto et al. (2012).

C. SIZES AND X-RAY LUMINOSITIES OF LMC SNRS

Table 1. Sizes and X-ray luminosities of LMC SNRs

| SNR J2000 ^a | Other Name | Size (Ba2010) (pc) | Size (De2010) (pc) | Size (Bo2017) (pc) | Large Discrepancy ^b (>16%) | Adopted Size (pc) | L_X^c (10^{35} ergs/s) |
|------------------------|---------------|-----------------------|-----------------------|-----------------------|--|----------------------|--------------------------------|
| J0448-6700 | [HP99] 460 | 55.0 | 59.2 | 60.8 | | 60.8 | 0.46 |
| J0449-6920 | – | 33.2 | 30.0 | 28.8 | | 28.8 | 0.07 |
| J0450-7050 | SNR 0450-70.9 | 89.2 | 97.5 | 109.4 | | 109.4 | 0.59 |
| J0453-6655 | SNR in N4 | 63.0 | 64.5 | 60.6 | | 60.6 | 1.17 |
| J0453-6829 | SNR 0453-68.5 | 30.0 | 30.0 | 30.4 | | 30.4 | 13.85 |
| J0454-6713 | SNR 0454-67.2 | 44.2 | 37.5 | 32.5 | | 32.5 | 1.58 |
| J0454-6626 | N11L | 21.8 | 18.0 | 20.4 | | 20.4 | 0.63 |
| J0455-6839 | N86 | 87.0 | 75.0 | 61.5 | Y | 61.5–75.0 | 1.42 |
| J0459-7008 | N186D | 37.5 | 36.8 | 29.0 | Y | 36.8 | 1.09 |
| J0505-6753 | DEM L71 | 18.0 | 20.2 | 18.6 | | 18.6 | 44.59 |
| J0505-6802 | N23 | 27.8 | 15.0 | 23.6 | Y | 23.6 | 26.25 |
| J0506-6541 | DEM L72 | 102.0 | 83.2 | 96.2 | | 96.2 | 0.53 |
| J0506-7026 | [HP99] 1139 | 82.5 | – | 42.5 | | 42.5 | 1.44 |
| J0508-6902 | [HP99] 791 | – | – | 67.0 | | 67.0 | 0.37 |
| J0508-6830 | – | – | – | 30.8 | | 30.8 | 0.09 |
| J0509-6844 | N103B | 7.0 | 7.5 | 7.0 | | 7.0 | 51.7 |
| J0509-6731 | SNR 0509-67.5 | 7.25 | 8.4 | 7.6 | | 7.6 | 16.51 |
| J0511-6759 | – | – | – | 55.5 | | 55.5 | 0.16 |
| J0512-6707 | [HP99] 483 | – | – | 12.5 | | 12.5 | 0.09 |
| J0513-6912 | DEM L109 | 53.8 | 57.8 | 55.6 | | 55.6 | 0.51 |
| J0514-6840 | – | – | – | 55.0 | | 55.0 | 0.4 |
| J0517-6759 | – | – | – | 66.8 | | 66.8 | 0.24 |
| J0518-6939 | N120 | 33.5 | 21.8 | 23.4 | | 23.4 | 0.88 |
| J0519-6902 | SNR 0519-69.0 | 7.8 | 8.2 | 8.6 | | 8.6 | 34.94 |
| J0519-6926 | SNR 0520-69.4 | 43.5 | 33.8 | 31.2 | | 31.2 | 2.69 |
| J0521-6543 | DEM L142 | – | 40.5 | 34.5 | | 34.5 | – |
| J0523-6753 | SNR in N44 | 57.0 | 52.5 | 57.5 | | 57.5 | 0.9 |
| J0524-6624 | DEM L175a | 58.5 | 51.8 | 36.25 | | 36.2 | – |
| J0525-6938 | N132D | 28.5 | 26.2 | 25.5 | | 25.5 | 315.04 |
| J0525-6559 | N49B | 42.0 | 36.0 | 38.8 | | 38.8 | 38.03 |
| J0526-6605 | N49 | 21.0 | 21.0 | 18.8 | | 18.8 | 64.37 |
| J0527-6912 | SNR 0528-69.2 | 36.8 | 35.2 | 35.0 | | 35.0 | 1.99 |
| J0527-6550 | DEM L204 | 75.8 | 67.5 | 76.2 | | 76.2 | – |
| J0527-6714 | SNR 0528-6716 | – | – | 54.0 | | 54.0 | 0.58 |

Table 1 continued

Table 1 (*continued*)

| SNR J2000 ^a | Other Name | Size (Ba2010) (pc) | Size (De2010) (pc) | Size (Bo2017) (pc) | Large Discrepancy ^b (>16%) | Adopted Size (pc) | L_X ^c (10^{35} ergs/s) |
|------------------------|---------------|-----------------------|-----------------------|-----------------------|--|----------------------|---|
| J0527-7104 | [HP99] 1234 | 49.0 | – | 70.2 | | 70.2 | 0.25 |
| J0528-6727 | DEM L205 | – | – | 55.0 | | 55.0 | 0.21 |
| J0529-6653 | DEM L214 | 25.0 | – | 33.1 | | 33.1 | 1.04 |
| J0530-7008 | DEM L218 | 53.2 | 47.2 | 49.4 | | 49.4 | 0.72 |
| J0531-7100 | N206 | 48.0 | 45.0 | 45.0 | | 45.0 | 2.55 |
| J0532-6732 | SNR 0532-67.5 | 63.0 | 67.5 | 45.0 | Y | 67.5 | 2.48 |
| J0533-7202 | – | – | – | 45.0 | | 45.0 | 0.57 |
| J0534-6955 | SNR 0534-69.9 | 28.5 | 23.2 | 28.8 | Y | 33.5 | 6.33 |
| J0534-7033 | DEM L238 | 45.0 | 40.5 | 47.5 | Y | 47.5 | 1.55 |
| J0535-6916 | SN 1987A | 0.5 | >1.5 | 0.45 | | 0.45 | 27.39 |
| J0535-6602 | N63A | 16.5 | 19.5 | 18.5 | | 18.5 | 185.68 |
| J0535-6918 | Honeycomb | 25.5 | 15.0 | 18.8 | Y | 15.0–25.5 | 0.4 |
| J0536-6735 | DEM L241 | 33.8 | 36.0 | 34.0 | | 34.0 | 3.84 |
| J0536-7039 | DEM L249 | 45.0 | 37.5 | 39.2 | | 39.2 | 1.43 |
| J0536-6913 | SNR 0536-69.2 | 120 | – | 16.5 | | 16.5 | 0.22 |
| J0537-6628 | DEM L256 | 51.0 | 48.0 | 46.9 | | 46.9 | 0.32 |
| J0537-6910 | N157B | 25.5 | 21.8 | 31.5 | Y | 21.8 | 15.0 |
| J0540-6944 | SNR in N159 | 19.5 | 27.0 | 26.2 | | 26.2 | 0.43 |
| J0540-6920 | SNR 0540-69.3 | 15.0 | 18.0 | 15.6 | | 15.6 | 87.35 |
| J0541-6659 | [HP99] 456 | – | – | 71.5 | | 71.5 | 0.77 |
| J0543-6858 | DEM L299 | 79.5 | 73.5 | 56.5 | Y | 56.5–73.5 | 1.68 |
| J0547-6943 | DEM L316B | 21.0 | 46.5 | 45.0 | | 45.0 | 1.47 |
| J0547-6941 | DEM L316A | 14.0 | 30.0 | 30.0 | | 30.0 | 1.26 |
| J0547-7025 | SNR 0548-70.4 | 25.5 | 28.5 | 28.1 | | 28.1 | 2.94 |
| J0550-6823 | – | 78.0 | 65.2 | 81.9 | Y | 81.9 | 1.22 |

^aThe 59 confirmed SNRs listed in Maggi et al. (2016).^bSize(De2010)/Size(Bo2017)>1.16 or <0.86.^cTaken from Maggi et al. (2016).